NEUROPHYSIOLOGY

Spatially structured inhibition defined by polarized parvalbumin interneuron axons promotes head direction tuning

Yangfan Peng[1†], Federico J. Barreda Tomas[2,3†], Paul Pfeiffer[3,4], Moritz Drangmeister[3,4], Susanne Schreiber[3,4‡], Imre Vida[2*‡], Jörg R.P. Geiger[1*‡]

In cortical microcircuits, it is generally assumed that fast-spiking parvalbumin interneurons mediate dense and nonselective inhibition. Some reports indicate sparse and structured inhibitory connectivity, but the computational relevance and the underlying spatial organization remain unresolved. In the rat superficial presubiculum, we find that inhibition by fast-spiking interneurons is organized in the form of a dominant super-reciprocal microcircuit motif where multiple pyramidal cells recurrently inhibit each other via a single interneuron. Multineuron recordings and subsequent 3D reconstructions and analysis further show that this nonrandom connectivity arises from an asymmetric, polarized morphology of fast-spiking interneuron axons, which individually cover different directions in the same volume. Network simulations assuming topographically organized input demonstrate that such polarized inhibition can improve head direction tuning of pyramidal cells in comparison to a "blanket of inhibition." We propose that structured inhibition based on asymmetrical axons is an overarching spatial connectivity principle for tailored computation across brain regions.

INTRODUCTION

Local excitatory synaptic connectivity between pyramidal cells (PCs) is sparse and specific (*1*, *2*), while perisomatic inhibition particularly by fast-spiking (FS), parvalbumin-positive interneurons (PV INs) is generally assumed to be dense and random (*3*). According to "Peters' rule," which suggests that axodendritic overlap determines synaptic connectivity (*4*, *5*), a "blanket of inhibition" could emerge from the overlap of a symmetrical, dense PV IN axon with neighboring neurons (*6*). Such inhibition could mediate gain control and maintain balance of excitation and inhibition (*7*–*9*).

This principle has been challenged by reports of nonrandom structured inhibitory connectivity in several brain regions (*10*–*12*), revealed by motif analysis applied to multineuron recordings (*13*). However, the determinants and the computational implications underlying these nonrandom network motifs are not yet resolved, as illustrated by the controversial debate on the role of PV IN connectivity for feature tuning in the visual cortex (*14*–*19*). Here, spatially organized connectivity between INs and PCs has recently been identified as a key principle for computation of direction selectivity (*20*). Whether such spatially structured inhibition is relevant for directional tuning in other cortical areas remains to be established.

The presubiculum (PrS) is the main cortical recipient of head direction (HD) information, integrating spatial and visual input from areas such as the anterodorsal thalamus, hippocampus, and retrosplenial cortex (*21*–*24*). It processes HD signals before passing them to the downstream medial entorhinal cortex (mEC), which are lastly critical for the generation of grid cell firing (*25*–*28*). HD and grid cell activity are hypothesized to rely on continuous attractor networks based on either recurrent excitation or inhibition (*29*–*33*). While such models use a specific connectivity in abstract feature spaces, they largely ignore constraints from the anatomical space. Recent studies have shown that spatially defined connectivity for HD in *Drosophila melanogaster* is implemented as a compass-shaped network (*34*). In addition, structured inhibition allows mapping of visual directional cues onto this HD circuit (*35*, *36*). Such direct correspondence between feature and anatomical space prompts the question of whether structured connectivity in mammals follows similar organizations (*37*).

As the superficial PrS exhibits prominent recurrent inhibition while lacking recurrent excitation (*32*, *38*), it is the ideal network to identify the organization principles of inhibitory connectivity and their impact on local HD computation. Therefore, we studied its connectivity, cellular anatomy, and computational capacity through multineuron patch-clamp recordings in combination with detailed morphological reconstructions. We found super-reciprocal motifs organizing perisomatic inhibition along a polarized PV IN axon morphology, a functional principle that also largely applies to other IN types. In spatial network simulations assuming topographically organized thalamic input, this specific structure-function principle demonstrated a stronger HD tuning of PCs than a blanket of inhibition.

RESULTS

Multipatch recordings reveal heterogeneous distribution of synaptic IN connections

In our previous study, we first described the network topology in the superficial PrS through multineuron patch-clamp recordings (*38*). In this study, we extended the analysis, focusing on 61 previously

[1]Institute for Neurophysiology, Charité—Universitätsmedizin Berlin, Corporate Member of Freie Universität Berlin, Humboldt-Universität zu Berlin, and Berlin Institute of Health, 10117 Berlin, Germany. [2]Institute for Integrative Neuroanatomy, Charité—Universitätsmedizin Berlin, Corporate Member of Freie Universität Berlin, Humboldt-Universität zu Berlin, and Berlin Institute of Health, 10117 Berlin, Germany. [3]Bernstein Center for Computational Neuroscience Berlin, Philippstr. 13, 10115 Berlin, Germany. [4]Institute for Theoretical Biology, Humboldt-Universität zu Berlin, 10115 Berlin, Germany.
*Corresponding author. Email: Joerg.Geiger@charite.de (J.R.P.G.); Imre.Vida@charite.de (I.V.)
†These authors contributed equally to this work.
‡These authors contributed equally to this work as co-senior authors.

recorded clusters (762 neurons), containing various INs and PCs patched in close proximity. Upon detailed examination, we found that while individual INs in these clusters presented reciprocal connections to multiple PCs, others lacked such high interconnectivity (Fig. 1, A and B). To further explore this apparent unequal distribution of connectivity, we separated the INs in groups with either zero, one, or more than one observed incoming or outgoing connection and counted these connections for each group. Out of 132 recorded INs in the superficial layers, 42% had zero connections, 20% had one connection, and 38% had more than one connection. The latter highly connected group of INs accounted for 87% (173 of 199) of all detected connections (Fig. 1D). Such a heterogeneous distribution could emerge from an IN subtype–specific connectivity. To rule out IN diversity as a major source for this heterogeneity, we analyzed FS

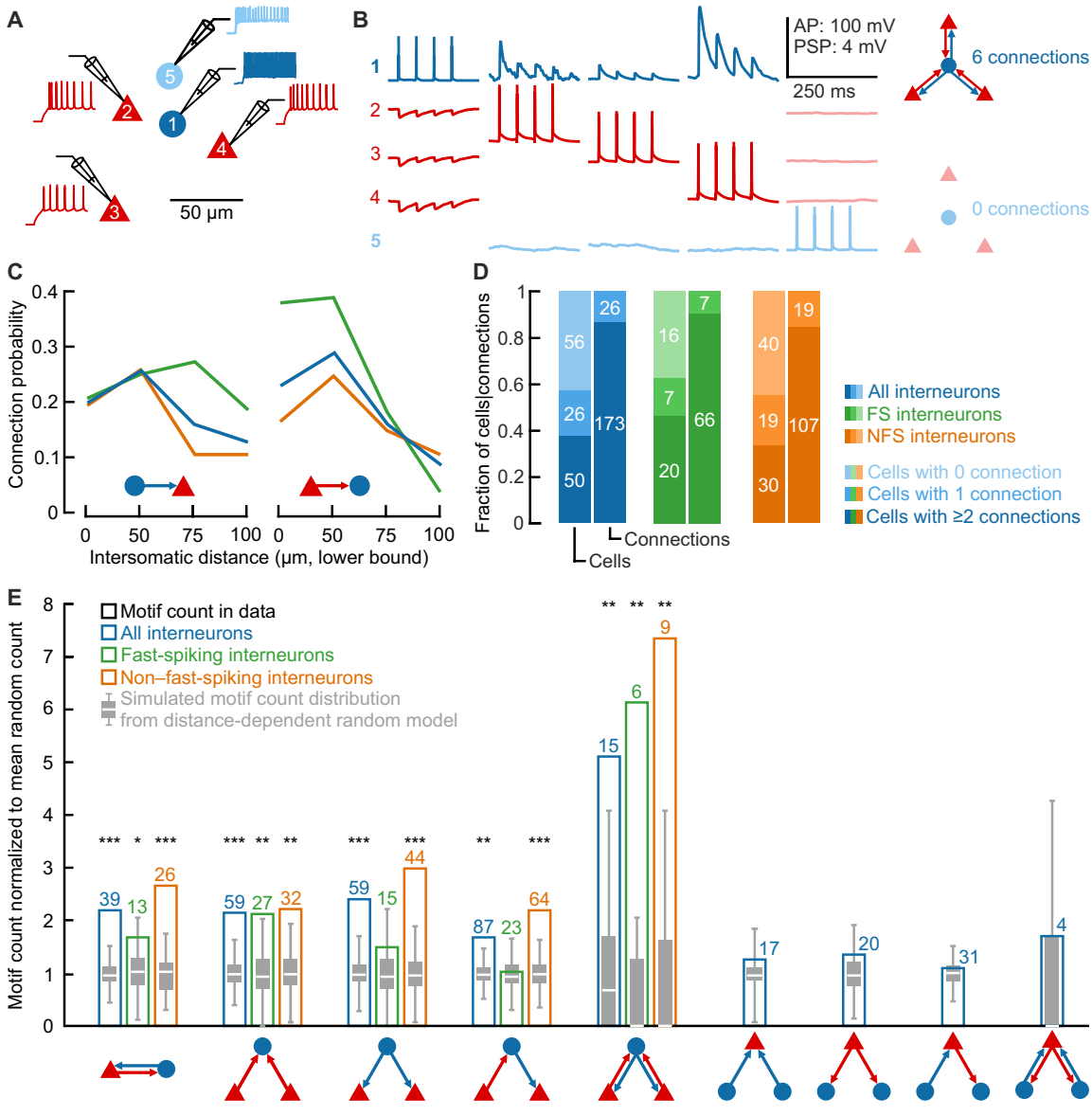

Fig. 1. Second-order motifs highlight recurrent inhibitory connectivity. (**A**) Schematic of a cluster of two INs (in blue) and three PCs (in red) with their firing patterns. (**B**) Matrix of current-clamp traces of neurons of the cluster. Four action potentials (AP) were evoked in each neuron consecutively to detect correlated postsynaptic responses in the other neurons. Dark blue and dark red traces indicate reciprocal connections of IN #1. Light red and light blue traces indicate absent connections of IN #5. PSP, postsynaptic potential. (**C**) Lines indicate the outgoing (left) and incoming (right) connection probabilities of all INs (blue), FS INs (green), and NFS INs (orange) for different distance bins (number of tested connections in each bin: 0 to 50 µm, $n = 96$; 50 to 75 µm, $n = 121$; 75 to 100 µm, $n = 100$; >100 µm, $n = 94$). (**D**) Stacked bar plots show the relative fraction of INs belonging to groups with either zero, one, or more than one connection (left bar). Numbers indicate the number of cells in each group. The adjacent bar shows the relative fraction of connections assigned to each group; numbers indicate the number of connections. (**E**) Gray box plots indicate the distribution of motif counts generated by the distance-dependent random model normalized to the mean random count; outliers beyond the whiskers are not visualized. Note that the random median count for the super-reciprocal motif for FS and NFS is zero due to its low probability and skewed random distribution. Framed colored bars indicate the ratio of observed motifs in the data relative to the mean number of simulated motifs for different subtypes of INs. Numbers above bars indicate the count of the respective motif in the dataset. *$P < 0.05$, **$P < 0.01$, and ***$P < 0.001$; see Materials and Methods for rank-based statistical test.

INs and non-FS (NFS) INs separately. The classification as FS was based on electrophysiological parameters trained on the PV staining of a subset of neurons (*38*). Regardless of whether the INs were FS ($n = 43$) or NFS ($n = 89$), we still observed that a minority of neurons of the respective subtype (FS, 47% and NFS, 34%) were responsible for most of the observed outgoing and incoming connections (FS, 90% and NFS, 85%; Fig. 1D). We further excluded that the probability of an IN being weakly or highly connected depended on the intersomatic distance or cell depth, i.e., soma distance to slice surface, and also excluded slice variability as the major cause for the inhomogeneous distribution (fig. S1). Together, the apparently skewed inhibitory connectivity is a feature of both IN subsets in the superficial PrS.

Presubicular INs form reciprocal connections with PCs constituting building blocks of a recurrent inhibitory network

To further investigate this heterogeneously distributed connectivity, we focused on the neurons with more than one connection and used an advanced motif analysis to quantify the occurrence of distinct connectivity patterns (*13*). We analyzed second-order motifs comprising any possible combination of two synaptic connections (inhibitory or excitatory and incoming or outgoing) made by an individual neuron (*10*, *39*). By comparing motifs from our dataset with simulations based on a distance-dependent random connectivity (*11*), we found that the reciprocal, convergent, divergent, and chain motifs involving a single IN with two PCs were significantly overrepresented (observed count versus mean random count ± SD: reciprocal, 39 versus 18 ± 4, $P < 0.001$; convergent, 59 versus 27 ± 7, $P < 0.001$; divergent, 59 versus 25 ± 7, $P < 0.001$; chain, 87 versus 52 ± 10, $P = 0.001$; see Materials and Methods for random simulation and statistical test; Fig. 1E). In contrast, complementary motifs involving a PC at the center and two INs as partners were found as often as expected in random simulations (convergent, 17 versus 15 ± 5, $P = 0.17$; divergent, 20 versus 15 ± 5, $P = 0.11$; chain, 31 versus 28 ± 6, $P = 0.29$; Fig. 1E). As the overrepresented second-order motifs can be combined into a specific super-reciprocal motif—one IN connecting reciprocally to two PCs—we investigated its occurrence in the dataset. We found 15 instances of this super-reciprocal motif, which is significantly more than expected (observed count versus mean random count: 15 versus 3, $P = 0.005$; Fig. 1E) and present in both IN subtypes (FS, 6 versus 1, $P = 0.008$; NFS, 9 versus 1, $P = 0.006$).

Together, we have found a prominent occurrence of specific recurrent inhibitory motifs in a subset of INs that does not arise from subtype-specific or distance-dependent connectivity. In contrast, a large fraction of INs does not seem to participate in the local microcircuit, which is biologically implausible. Therefore, we hypothesize that this could result from a deviation of the principle of blanket of inhibition. The observed unequal distribution of IN connectivity may arise from a specific directional axon morphology and the sampling bias of our multipatch approach that provides recordings from one geometrical plane. To investigate this hypothesis in a homogeneous population of INs with regard to morphology, physiology, and molecular profile, we primarily focused on PV-positive FS cells.

Overlap of PCs with an asymmetrical PV IN axon determines synaptic connectivity

We performed additional recordings from FS INs and confirmed their neurochemical identity through immunolabeling against PV. We showed that almost all were PV positive (28 of 32 recorded FS INs, 15 in cluster, 12 in paired, and 5 in single-cell configuration). In these experiments, we recorded clusters with multiple PCs but only a single IN, optimized to obtain detailed three-dimensional (3D) reconstructions (see Materials and Methods and Fig. 2A). The axonal arbor of reconstructed PV INs exhibited dense areas of collaterals nonuniformly distributed around the PV-positive cell body (Fig. 2A). We calculated the density distribution of the axonal arbor (Fig. 2B) and observed substantial differences in its overlap with PC dendrites and cell bodies (Fig. 2D and fig. S2A). Since this heterogeneity in axodendritic overlap likely determines local connectivity between PV IN and PCs, we calculated an axonal overlap score based on the colocalization of soma and dendrites of PCs with the PV IN axon.

We found that pairs with inhibition, including those with reciprocal excitation, were associated with a high axonal overlap score (overlap score > 0.1; Fig. 2E). In contrast, pairs with no inhibition showed a low overlap score (overlap score < 0.1; Fig. 2E). This pattern of inhibitory connectivity is in good agreement with Peters' rule. We observed that pairs with high IN axonal overlap scores also exhibited a markedly higher excitatory connectivity (high versus low overlap: 69% versus 19%, $P = 0.002$, Fisher's exact test; Fig. 2F). Furthermore, most excitatory connections were found in the presence of inhibition (71% versus 16%, $P < 0.001$; Fig. 2F). We hence hypothesize that the establishment of excitatory connections is largely promoted by the inhibitory connectivity and the underlying IN axonal overlap, forming the basis for the overrepresented super-reciprocal motif found in the network (Fig. 1C).

Presubicular PV INs exhibit a polarized morphology oriented toward different directions

To further investigate the asymmetrical axonal distribution, we reconstructed PV INs from L2/3 of the mEC ($n = 10$), which also contains spatially modulated cells but exhibits a dense and random inhibitory connectivity (*29*, *40*), and compared their axonal morphology to our set of presubicular PV INs ($n = 10$). Visual examination indicated that presubicular PV IN axons showed a polarized spatial distribution in contrast to a more radially symmetrical axon of mEC PV INs (Fig. 3A and fig. S2, B and C). To quantify these differences, we generated 3D polar plots, from which we could calculate measures of the axons' deviation from a spherical shape: a polarity index and the measure of eccentricity. Both of these demonstrated that axons of PV INs in the PrS had a more polarized structure than in the mEC (polarity index PrS versus mEC, means ± SD: 10.5 ± 3.6 versus 6.5 ± 2.8, $P = 0.007$; eccentricity: 0.7 ± 0.1 versus 0.5 ± 0.1, $P = 0.009$, Mann-Whitney U test; Fig. 3B). The finding of axonal polarization poses the question of whether all PV INs are aligned in the same direction or whether there is a broad distribution of orientations. To address this question, we recorded and filled six pairs of neighboring PV INs in five slices of the PrS (Fig. 3C). Reconstructions of these pairs revealed that the long axes of the polarized axons showed independent orientations (Fig. 3C). Moreover, when the polar plots for 12 PV INs were superimposed (7 from cluster, 2 from paired, 3 from single-cell recordings), aligned according to anatomical landmarks, the axonal distributions evenly covered all directions in 3D space (Fig. 3D). In summary, while the axons of individual PV INs show a high level of polarization, at the population level, they can mediate perisomatic inhibition across the presubicular space by covering all possible directions.

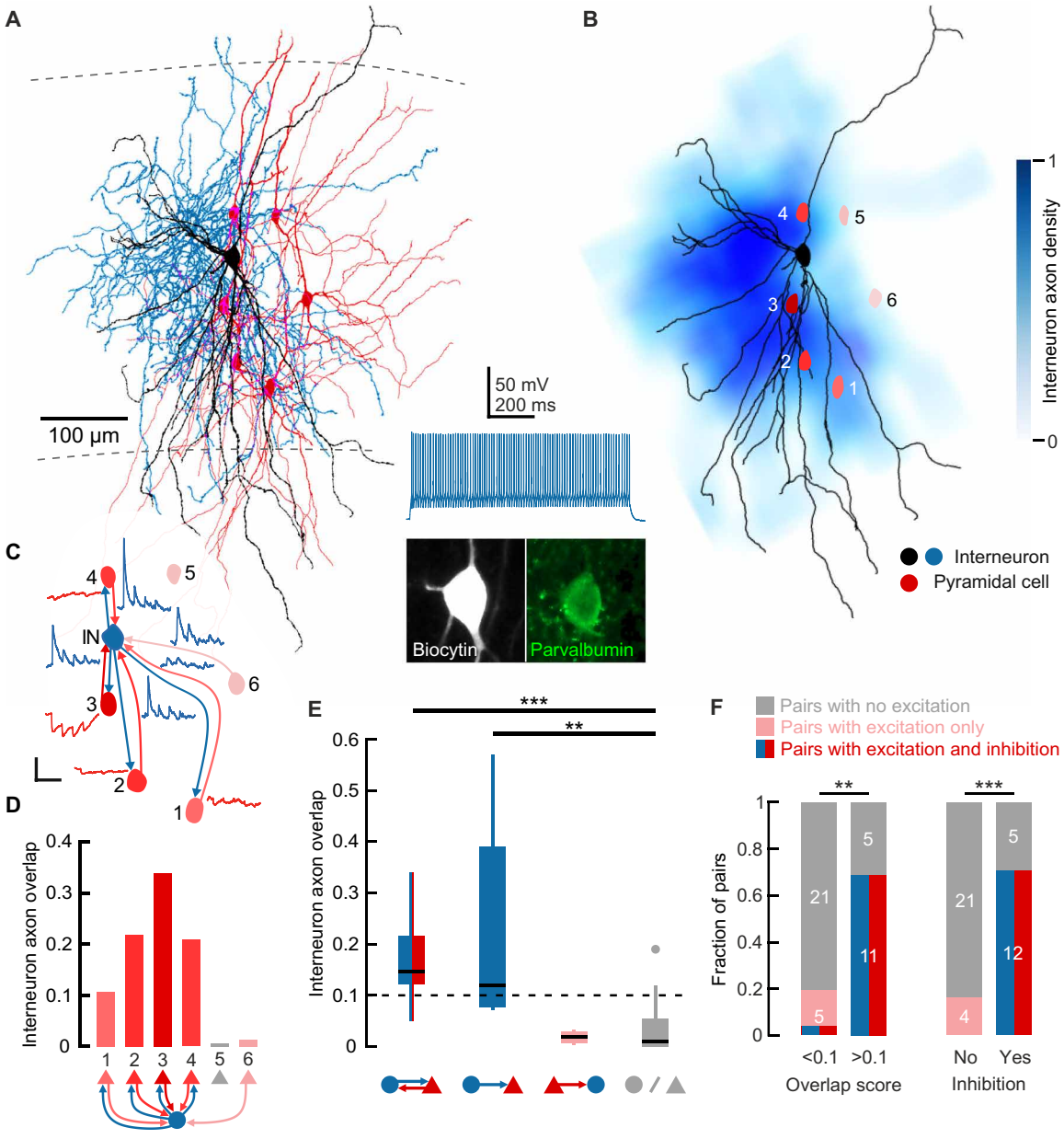

Fig. 2. Spatial overlap of PV IN axon and PC somato-dendritic domain correlates with synaptic connectivity. (**A**) Representative reconstruction of a biocytin-filled cluster composed of a single PV IN (soma and dendrites in black and axon in blue) and six PCs (in red, without axon). Inset (top): FS firing pattern elicited by step current stimulation. Inset (bottom): High-magnification confocal image of the biocytin labeling (white) (left) and PV immunological signal (green) in the IN soma (right). (**B**) Density distribution of the PV IN axon (blue gradient) superimposed on the reconstruction of the IN soma and dendrites (in black) and PC somata (red gradient). (**C**) Scheme depicting synaptic connections and corresponding postsynaptic responses recorded from neurons of the cluster in (A). Excitatory connections are in red, and inhibition is in blue. Scale bars, 100 ms (horizontal) and 1 mV (vertical). (**D**) Bar graph of the IN axon overlap scores for the PCs. Synaptic connections of the PCs with the PV IN are schematically illustrated below the *x* axis. (**E**) Summary box plots of the overlap scores for the PC-PV IN pairs from all recorded clusters. The bars represent pairs with reciprocal connection (blue/red, $n = 12$), only inhibition (blue, $n = 5$), only excitation (light red, $n = 4$), or without connections (gray, $n = 21$). Dotted line indicates the threshold of 0.1 separating high and low overlap scores, $^{**}P < 0.01$ and $^{***}P < 0.001$, Mann-Whitney *U* test. (**F**) Stacked bar plots show the fraction of excitatory connections (light red, only excitation; red/blue, excitation and inhibition) among pairs with low versus high overlap scores (left pair of bars) and among pairs with inhibitory connection versus those lacking inhibitory connection (right pair of bars). Numbers indicate absolute counts of pairs in these groups. $^{**}P < 0.01$ and $^{***}P < 0.001$, Fisher's exact test.

Polarized morphology and overlap-dependent connectivity rule also largely applies to the heterogeneous group NFS INs

To investigate whether the same structure-function principle applies to NFS INs, we reconstructed recorded clusters with a single NFS IN and multiple PCs and calculated the IN axonal overlap scores of these pairs (fig. S3, A and B). Consistent with the findings for FS PV INs, inhibitory connections by NFS INs were associated with a high overlap score, whereas pairs with no connections showed low scores (reciprocal and unidirectional inhibitory versus not connected pairs, means ± SD: 0.35 ± 0.3 versus 0.03 ± 0.02, $P < 0.001$,

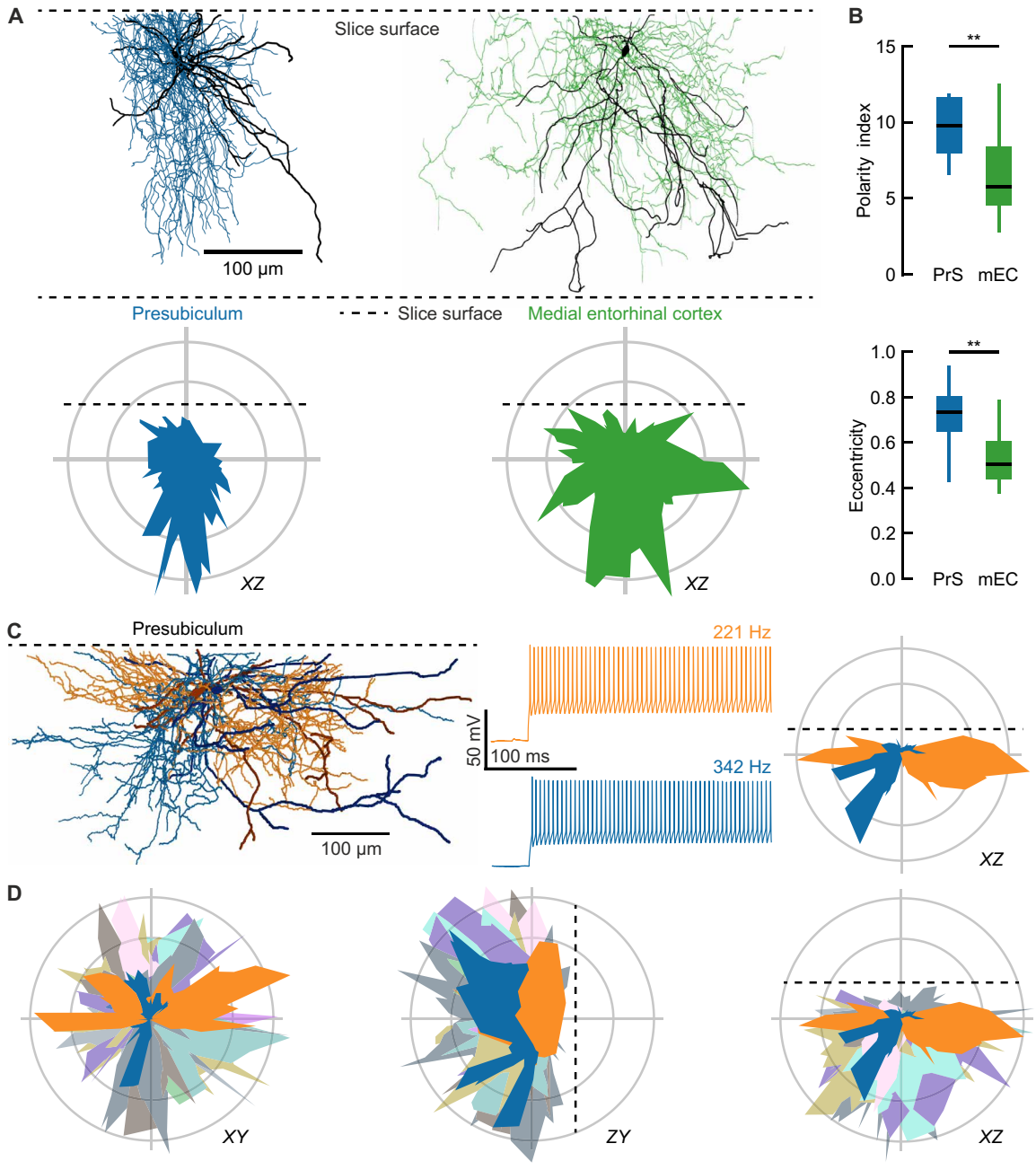

Fig. 3. Presubicular PV INs present polarized axon morphologies with distinct orientations. (**A**) Top: 3D reconstructions of a biocytin-filled presubicular PV IN (soma and dendrites in black), with a polarized axon (in blue) and a PV IN from the mEC with a circular axonal distribution (in green), viewed from the pial surface. Dotted lines indicate cut slice surface. Bottom: Polar plots (bottom) of the axonal distribution binned at 10°. (**B**) Box plots show polarity index (top) and eccentricity (bottom) for PrS ($n = 12$) and mEC IN axons ($n = 16$, $^{**}P < 0.01$, Mann-Whitney U test). (**C**) Left: 3D reconstruction of two neighboring presubicular PV INs viewed from the pia (axons in blue and orange). Inset (middle): Firing patterns of the two PV INs elicited by step current stimulation with frequency indicated in the respective color. Right: Corresponding polar plot of the IN axons highlights their near-orthogonal orientation in the slice. (**D**) Summary polar plots of presubicular PV IN axons [pair from (C) and additional 10 PV INs, total $n = 12$] viewed from three perspectives in 3D space. Dotted lines indicate the slice surface.

Mann-Whitney U test; fig. S3B). Similarly, a high axonal overlap score was also associated with a higher excitatory connectivity (high versus low overlap: 50% versus 6%, $P = 0.007$, Fisher's exact test; fig. S3C). Despite representing a more heterogeneous group, the axon morphology of NFS INs also exhibited strong polarization, as found in PV INs (polarity index NFS versus FS, means ± SD: 11.1 ± 7.9 versus 10.5 ± 3.6; eccentricity: 0.7 ± 0.1 versus 0.7 ± 0.1). Superimposed polar plots aligned to anatomical landmarks also showed that NFS IN axons are broadly distributed along directions in 3D space (fig. S3E). These findings indicate that the identified structure-function principle is not only exclusive to PV INs but can also be extrapolated to INs of the diverse NFS group.

Super-motifs organized along polarized PV IN axons prompt a computational comparison of different network architectures

Following the structure-function connectivity principle established experimentally, we constructed spatial network models implementing structured recurrent inhibitory connectivity constrained along the extent of the respective perisomatic inhibitory IN axon. We simulated the postprocessing of HD input inherited from the upstream anterodorsal thalamic nucleus, a prominent function of the PrS. The spatial organization of the thalamic input is as of yet unknown; therefore, we modeled the topography of HD preference among PCs by Perlin (simplex) noise (Fig. 4A). This allowed us to vary forms of input organization between "salt-and-pepper"–like and more structured maps (fig. S4C). For the spatial network, we placed 3600 PCs and 400 INs on a uniformly spaced grid onto a 2D neural sheet (900 μm by 900 μm) and connected the cells according to the empirically observed connectivity rule (Fig. 4B): PCs within the spatial reach of axonal clouds of a neighboring IN were connected reciprocally. For the network with spatially structured inhibition, we considered polarized IN axons that were approximated by an ellipsoid shape with a long axis of 200 μm and a short axis of 50 μm (Fig. 4B, left), resembling the morphological reconstructions of PV INs. Each IN could thus target a specific subset of neighboring PCs defined by its orientation relative to the thalamic input structure. In the model, we assumed that the ellipsoids are oriented to maximize the diversity of HDs within their spatial reach (see Materials and Methods and fig. S4A). As a comparison, we constructed a blanket of

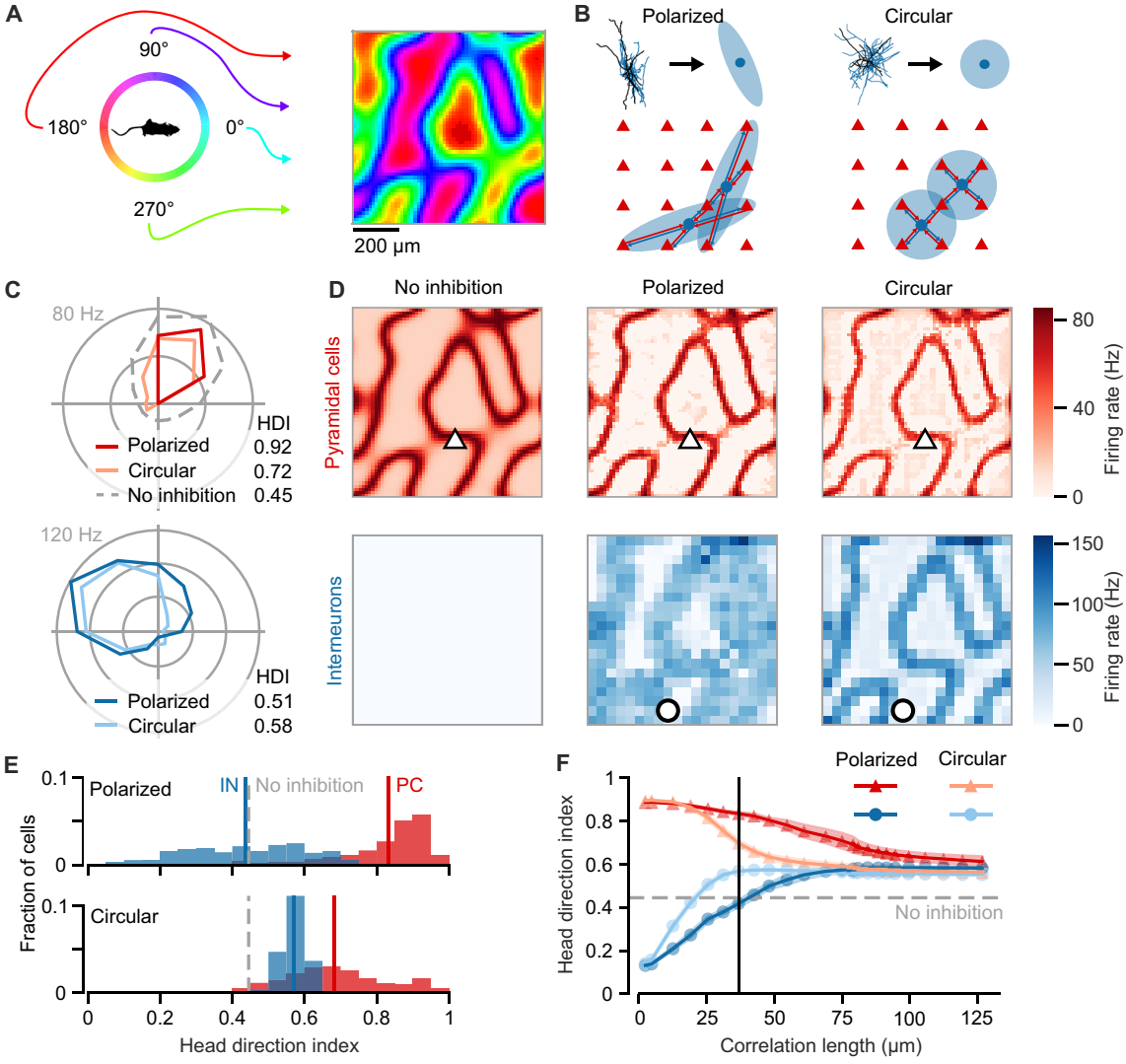

Fig. 4. Comparison of polarized and circular IN axon morphology in a spatial network model. (**A**) Topography of HD preference (colors) among PCs in a model of the PrS superficial layers is simulated by 2D simplex noise. (**B**) Spatial network connectivity is determined by either a polarized or circular IN morphology. Polarized INs are oriented to maximize the diversity of HD preferences among connected PCs. Area-equivalent circular INs model an unspecific blanket of inhibition. (**C**) Firing rates for different HDs and HDIs of an exemplary PC [triangle in (**D**)] and IN [circle in (D)] in the networks of polarized (dotted) and circular (solid) INs. Spatial maps of firing rates among PCs (top) and INs (bottom) for networks with no inhibition, polarized, and circular INs provided with exemplary HD input at 0°. (**E**) Distribution of HDI of all PCs (red) and INs (blue) in the above networks with either polarized (top) or circular (bottom) INs. Thick lines indicate the mean HDI of the respective neuron population (polarized: PC, 0.83 and IN, 0.44; circular: PC, 0.68 and IN, 0.57). (**F**) Mean HDI of PCs (red) and INs (blue) in network models with polarized (dark) or circular (light) INs for HD input topographies of different correlation lengths (see fig. S4). Vertical line indicates the correlation length (37 μm).

inhibition network with area-equivalent circular IN axons of 100 μm diameter. We analyzed the different network models to explore the potential computational advantage of the microcircuit architecture found in the PrS versus a blanket of inhibition.

Simulation of network activity for different HDs reveals that ellipsoid axonal clouds mediate stronger tuning than circular axons

Polarized INs suppressed PC firing more effectively at nonpreferred HDs and less at preferred HDs compared to circular INs, improving the signal and reducing the noise, thereby increasing the HD index (HDI) (Fig. 4C and fig. S4B). At the network level, this resulted in sharper boundaries between PC populations with different HD preferences on the neural sheet in the model with polarized INs in contrast to the blanket of inhibition model with circular INs (Fig. 4D). Polarized INs themselves developed a broader HD tuning compared to circular INs as they sampled from more diversely tuned PCs (Fig. 4, C and D). Thus, the disparity in HD tuning between PCs and INs was substantially increased in networks with polarized compared to circular axon morphology (Fig. 4E). The difference in HD tuning via polarized INs depended on the relationship of the spatial scale of the input topography to the size of the IN axonal clouds rather than on the specific input map [see Materials and Methods and fig. S4 (D to F) for an alternative input map]. Notably, we observed that the polarized model outperformed the circular model at correlation lengths between 25 and 100 μm, the upper end corresponding to approximately half of the long axis of the ellipsoid axons (Fig. 4F). Together, our simulations indicate that, for a topographically organized HD input, polarized perisomatic inhibition via PV INs can improve computational performance.

DISCUSSION

In this study, we have identified a previously unknown spatial connectivity principle of recurrent inhibition in the PrS of the rat. Microcircuits of the PrS are dominated by super-reciprocal connectivity motifs organized by the polarized axons of PV INs. The individual directions of these axons constrain the interaction of PV INs to specific subsets of PCs. Thus, multiple subnetworks can be oriented toward different directions within a given anatomical space. We investigated the role of this network principle in the context of HD representation, which has been widely described in vivo in the PrS (*25*, *26*). Our simulations demonstrate a substantial advantage of this spatial connectivity rule for the tuning of HD activity given a topographical organization of HD input. The combined effort of multineuron patch-clamp recordings, detailed 3D morphological analysis, and spatial network simulations identified a spatially defined connectivity principle that carries implications for microcircuit computation.

A blanket of inhibition by PV INs is generally assumed in cortical areas and relies on symmetrical axon distributions as well as a dense formation of synapses according to Peters' rule (*3*, *6*). This concept further explains random reciprocal connectivity between PV INs and PCs (*18*, *29*, *41*). Dense inhibition and random reciprocity have also been described in the mEC, a region downstream to the PrS (*29*, *40*). In the PrS, we identified that the spatial extent of polarized IN axon morphology underlies the prominent reciprocity between PCs and PV INs. Our findings highlight that PV INs can target a specific subset of neurons by directing their axonal projections without violating Peters' rule. However, the fact that PV IN axonal overlap also predicted the reciprocal excitation by inhibited PCs indicates additional mechanisms that govern local IN excitation. The tuning of morphology and aligned connectivity likely involve further mechanisms, such as developmental (*42*) or activity-dependent plasticity (*43*).

Thus, spatial organization of inhibition allows function-specific connectivity. In the visual cortex, connections are preferentially established between similarly tuned neurons that serve either feature amplification (*44*) or redundancy reduction (*45*). While evidence for the role of PV INs in tuning of visual input has been controversial (*14*–*19*), a recent study has demonstrated that the spatial offset between PCs and INs is directly linked to the tuning of direction selectivity (*20*). However, the corresponding axodendritic morphology and the contribution of PV INs are not resolved. Polarized IN axons, as found here, can represent a potential anatomical solution to spatially organized function-specific connectivity. In *Drosophila*, mapping of visual cues onto the HD circuit relies on spatially structured inhibition (*35*). Our results suggest a similar integration of allocentric visual information with HD signals supported by structured inhibition in the mammalian PrS (*22*, *46*). Thus, spatially defined inhibitory connectivity could represent an overarching principle to encode and integrate directionality of external and internal stimuli.

Since the organization of thalamic and retrosplenial input to the PrS is still unknown (*21*), we used different topographical input maps to explore the potential advantage of the modeled polarized INs for feature computation. In contrast to radially symmetrical axons, polarized axons can sample selectively from neighboring PCs. INs connecting to PCs with more diverse HD preferences can enhance the directional tuning of the individual PCs. As a further consequence, polarized INs become more broadly tuned, as they sample from diverse HDs, in line with prior reports showing broad tuning of FS INs within the PrS in vivo (*25*, *26*). The observed polar morphology provides a means by which local IN tuning could differ substantially from a simple average of the surrounding PCs as previously suggested (*8*). Specifically, we postulate that the broad HD tuning of INs in vivo emerges from selective sampling of their surrounding HD PCs. This hypothesis and the underlying assumptions, such as the spatial organization of HD input, should be addressed through future in vivo high-density electrode recordings (*22*).

IN subtypes within the PrS receive distinct thalamic input and exhibit various forms of synaptic dynamics, suggesting different roles in HD computation (*27*, *32*). However, the reported spatially asymmetric connectivity rule is not restricted to PV-positive INs but rather applies to PrS INs in general. Thus, our model focused on the ability of polarized IN axon morphology to structure connectivity and thereby improve HD tuning. How diverse IN types in the PrS with their structured connectivity contribute specifically to HD and other spatial computations remains to be investigated.

Together, we identified a principle for structured inhibitory connectivity that helps to bridge the gap between anatomical and feature space. The microcircuit organization of the PrS exemplifies a deviation from a blanket of inhibition paradigm that can be leveraged for improved computation. Thus, we propose that anatomically structured inhibition can offer area-specific tailored computations (*47*).

MATERIALS AND METHODS

Animals

Patch-clamp recordings and morphological reconstructions were performed on acute brain slices obtained from 19- to 35-day-old

transgenic Wistar rats expressing Venus–yellow fluorescent protein (YFP) under the vesicular gamma-aminobuteric acid transporter (VGAT) promoter (*48*). Animal handling and all procedures were carried out in accordance with the guidelines of local authorities (Berlin, T0215/11 and T0109/10), the German Animal Welfare Act, and the European Council Directive 86/609/EEC.

Multineuron patch-clamp recordings

For the extended network motif analysis, we reanalyzed our previously published dataset on synaptic connectivity obtained through multineuron patch-clamp (multipatch) recordings in the PrS (*38*). As the superficial layer lacks recurrent excitatory connections, it represents an ideal system to study recurrent inhibitory connectivity principles. Thus, we focused on 61 clusters with up to eight neurons recorded in the superficial layer (distance to pia, <600 μm). For details on motif analysis and random simulation, see data analysis.

To correlate detailed morphological reconstructions with electrophysiological detection of synaptic connectivity, we performed additional multipatch recordings with optimized intracellular solutions as previously reported (*38*): Animals were anesthetized with isoflurane and decapitated. The head was submerged in cold artificial cerebrospinal fluid (ACSF) slicing solution containing 80 mM NaCl, 2.5 mM KCl, 3 mM $MgCl_2$, 0.5 mM $CaCl_2$, 25 mM glucose, 85 mM sucrose, 1.25 mM sodium phosphate buffer (PB), and 25 mM $NaHCO_3$ (320 to 330 mOsm), enriched with carbogen (95% O_2 and 5% CO_2). Horizontal 300-μm-thick slices 4 to 5.5 mm above the interaural plane were cut on a Leica VT1200 vibratome (Leica Biosystems) and then stored in the slicing solution under submerged condition heated to 30°C for 30 min of recovery. After the recovery, slices were stored in the oxygenated slicing solution for up to 5 hours at room temperature. Patch-clamp recordings were performed in a submerged recording chamber perfused with ACSF solution (34°C) containing 125 mM NaCl, 2.5 mM KCl, 1 mM $MgCl_2$, 2 mM $CaCl_2$, 25 mM glucose, 1.25 mM sodium PB, and 25 mM $NaHCO_3$ (310 to 320 mOsm), enriched with carbogen (95% O_2 and 5% CO_2). Somatic whole-cell patch-clamp recordings were performed with pipettes pulled from borosilicate glass capillaries with 2 mm outer diameter and 1 mm inner diameter (Hilgenberg, Germany) on a horizontal puller (P-97, Sutter Instrument Company). The pipettes were filled with intracellular solution containing 130 mM K-gluconate, 6 mM KCl, 2 mM $MgCl_2$, 0.2 mM EGTA, 5 mM Na_2-phosphocreatine, 2 mM Na_2ATP, 0.5 mM Na_2GTP, and 10 mM Hepes buffer (290 to 300 mOsm, pH adjusted to 7.2 with KOH). To enhance contrast between biocytin staining of INs and PCs, we added biocytin (0.7 mg/ml) for IN recordings and biocytin (0.1 mg/ml) for PC recordings. Filled pipettes had a resistance of 3 to 7 megohms. We did not correct membrane potentials for liquid junction potential. Cells were visualized through an infrared differential interference contrast microscope (Olympus BX-51WI) equipped with a digital camera (Olympus XM10). INs were selected before patching by their VGAT-YFP fluorescence observed in epifluorescence illumination using a 490-nm light-emitting diode (LED) light source (Thorlabs). We recorded from up to eight cells simultaneously, selecting cells up to a depth of 80 μm beneath the slice surface. Series resistance of the recordings was compensated using the automatic bridge balance of the amplifier. Recordings were performed using four two-channel MultiClamp 700B amplifiers (Molecular Devices) in current-clamp mode. Data were low-pass filtered at 6 kHz using the amplifiers built in Bessel filter and digitized with a Digidata 1550 (Molecular Devices) at a sampling rate of 20 kHz. The pClamp 10.4 software package (Molecular Devices) was used for data acquisition and analysis. To detect monosynaptic connections, we applied the same protocols as in our previous study (*38*). In brief, we elicited four action potentials in each recorded neuron consecutively by injecting 1- to 2-ms current pulses of 1 to 2.5 nA. Individual neurons were held in current-clamp mode and stimulated sequentially in 1-s intervals. Between 40 and 50 sweeps were averaged for the analysis. Monosynaptic connections were identified when excitatory or inhibitory postsynaptic potentials were tightly correlated with the elicited presynaptic action potential within a latency of 3 ms.

Network motif analysis

Motif counting and random simulation

Motif analysis was performed using custom MATLAB-based scripts (https://doi.org/10.5281/zenodo.4670433). We summed the number of second-order motifs from all neurons that were calculated on the basis of the incoming and outgoing connections of each neuron to the respective partner cell types (*39*)

$$\text{Number of convergent motifs} = \frac{\text{Connection}_{\text{in}} * (\text{Connection}_{\text{in}} - 1)}{2}$$

$$\text{Number of divergent motifs} = \frac{\text{Connection}_{\text{out}} * (\text{Connection}_{\text{out}} - 1)}{2}$$

$$\text{Number of chain motifs} = (\text{Connection}_{\text{in}} * \text{Connection}_{\text{out}}) - \text{Connection}_{\text{reciprocal}}$$

$$\text{Number of double reciprocal motifs} = \frac{\text{Connection}_{\text{reciprocal}} * (\text{Connection}_{\text{reciprocal}} - 1)}{2}$$

To determine whether these motifs occurred significantly more often than expected by chance, we simulated 50 recorded clusters with the same configuration (14 octuples, 6 septuples, 14 sextuples, 8 quintuples, 3 quadruplets, and 5 triplets), cell types (226 PCs and 114 INs), and *XY* coordinates (11 of 61 recorded clusters from the superficial layer were excluded due to missing coordinates) 10,000 times assuming randomly distributed distance-dependent connectivity (*10*, *11*). The connection probability for each independently established connection at the specific intersomatic distance was determined by the number of found connections divided by the number of tested connections of the respective connection type in the respective distance bin (0 to 50, 50 to 75, 75 to 100, and >100 μm; Fig. 1C) as reported previously (*38*). We counted the number of second-order motifs from each of these simulations with the same approach and compared the number of simulated motifs with the number of found motifs from the empirical dataset.

Statistical comparison and multiple hypothesis correction

P values for statistical comparison between empirically found motifs and simulated motifs were calculated according to previous studies (*10*, *11*). For each motif, we divided the number of simulations of our dataset that yielded a higher motif count than the empirically observed motif count by the number of total simulations (10,000). This represents the *P* value indicating the probability of the null hypothesis being true (H_0: "The observed motif count is equal or lower to the predicted motif count by the random simulations"). If a motif never occurred in the simulation, we set the motif count to 1,

which resulted in a P value of 0.0001. To correct for testing multiple hypotheses, we applied the Benjamini-Hochberg method, which controls for the false discovery rate (*49*). We sorted the P values for n comparisons in ascending order ($P_1 < P_{i...} < P_n$). The first P value at position i with a lower value than $i/n * \alpha$ was deemed statistically significant at the α level ($\alpha = 0.05$). All comparisons with P values lower than P_i were also considered as statistically significant.

Single-cell patch-clamp recordings

Single presubicular INs were recorded for the comparative polarity assessment, as well as the axonal orientation analyses (Fig. 3, A and C). For this, animals were anesthetized (3% isoflurane, Abbott, Wiesbaden, Germany) and then decapitated. Brains were quickly removed and transferred to carbogenated (95% O_2/5% CO_2) ice-cold sucrose ACSF containing 87 mM NaCl, 2.5 mM KCl, 25 mM $NaHCO_3$, 1.25 mM sodium PB, 25 mM glucose, 75 mM sucrose, 7 mM $MgCl_2$, 0.5 mM $CaCl_2$, 1 mM Na-pyruvate, and 1 mM ascorbic acid. Horizontal brain slices (300 μm thick) were cut using a vibratome (VT1200 S, Leica, Wetzlar, Germany). Slices were collected and placed in a submerged holding chamber filled with carbogenated sucrose ACSF at 32° to 34°C for 30 min and then at room temperature until recording. For recording, slices were transferred to a submerged chamber and superfused with carbogenated ACSF containing 125 mM NaCl, 2.5 mM KCl, 25 mM $NaHCO_3$, 1.25 mM sodium PB, 25 mM glucose, 1 mM $MgCl_2$, 2 mM $CaCl_2$, 1 mM Na-pyruvate, and 1 mM ascorbic acid. The bath temperature was set to 32° to 34°C with a perfusion rate of 12 to 13 ml/min. Slices were visualized using an upright microscope (BX-51WI; Olympus) equipped with infrared differential inference contrast optics and a digital camera (Zyla CMOS, Andor, UK). INs were identified by their VGAT-YFP signal visualized by epifluorescent illumination delivered via a fixed-wavelength LED source ($\lambda = 514$ nm, OptoLED, Cairn Research, UK). A dataset of single L2/3 FS INs of the mEC was reanalyzed to serve as a control population for the polarity assessment in this study (*40*). For the orientation analysis, respectively two neighboring INs in close proximity (<200 μm) in L2/3 of the PrS were recorded and biocytin-filled. Whole-cell patch-clamp recordings were conducted with electrodes from borosilicate glass capillaries (outer diameter, 2 mm; inner diameter, 1 mm; Hilgenberg, Germany) produced by a horizontal puller (P-97, Sutter Instruments, CA, USA) and filled with an intracellular solution consisting of 130 mM K-gluconate, 10 mM KCl, 10 mM Hepes, 10 mM EGTA, 2 mM $MgCl_2$, 2 mM Na_2ATP, 0.3 mM Na_2GTP, 1 mM Na_2-creatine, and 0.1% biocytin (adjusted to pH 7.3 and 315 mOsm), giving a series resistance of 2.5 to 4 megohms. All recordings were performed with an Axopatch 700B amplifier (Molecular Devices, CA, USA), filtered online at 10 kHz with the built-in two-pole Bessel filter, and digitized at 20 kHz (National Instruments, UK). Following breakthrough into whole-cell configuration, we characterized the firing properties in current-clamp mode using hyper- to depolarizing current pulses (a family of −500 to 500 pA in 100-pA steps, followed by a single step to 1.2 nA, 1000-ms duration). Cells were excluded if the resting membrane potential was more depolarized than −45 mV, initial series resistance of >30 megohms, or >20% change occurred in series resistance over the course of the recording. The liquid junction potential was not corrected. Electrophysiological data were acquired online using the open-source WinWCP software package (courtesy of J. Dempster, Strathclyde University, Glasgow, UK; http://spider.science.strath.ac.uk/sipbs/software_ses.htm).

Visualization of recorded neurons and PV immunocytochemistry

Slices were immersion-fixed in a solution containing 4.5% paraformaldehyde, 4% sucrose and 0.1 M PB (pH 7.4) for a minimum of 12 hours (overnight) at 4°C. Slices were then rinsed extensively in 0.1 M PB followed by phosphate-buffered saline (PBS; 0.9% NaCl). For visualizing the biocytin-filled neurons, slices were incubated in a solution containing avidin-conjugated Alexa Fluor 647 (dilution 1:1000; Invitrogen, Darmstadt, Germany) in PBS with 3% normal goat serum (NGS), 0.1% Triton X-100, and 0.05% NaN_3 overnight. For immunological staining for PV, slices were first blocked in PBS containing 10% NGS, 0.3% Triton X-100, and 0.05% NaN_3 for 1 hour and afterward incubated with a polyclonal rabbit anti-PV antibody (1:2000; Swant, Switzerland) in PBS containing 5% NGS, 0.3% Triton X-100, and 0.05% NaN_3 for at least 72 hours at 4°C. Slices were then rinsed, and a fluorescent-conjugated secondary antibody was applied (1:1000; goat anti-rabbit immunoglobulin G, Alexa Fluor 405, Invitrogen, UK) in a PBS solution containing 3% NGS, 0.1% Triton X-100, and 0.05% NaN_3 overnight at 4°C. Slices were then mounted in an aqueous mounting medium (Fluoromount-G, Southern Biotech) on 300-μm-thick metal spacers to prevent shrinkage in the z plane.

Imaging of the slices was performed on a confocal laser scanning microscope (FluoView FV1000, Olympus, Japan). First, a low-magnification (×4 air immersion, Olympus, Japan) overview image was taken to confirm the cellular localization, following a high-magnification z stack using a 30× silicon oil immersion objective [numerical aperture (NA) of 1.05, UPlanSApo, Olympus] for morphological assessment of biocytin-labeled neurons, using a 643-nm diode laser to excite the avidin-conjugated Alexa Fluor 647. To confirm PV neurochemical identity and YFP immunoreactivity of recorded cells, a high-magnification image (60× objective, NA of 1.2, Olympus, Japan) was taken over the soma and proximal dendrites. We used a 488-nm argon laser for fluorescent excitation of YFP and a 405-nm diode laser for excitation of the Alexa Fluor 405–conjugated secondary antibody. Images were analyzed offline; for details on 3D reconstruction and analysis, consult the "Morphological analysis" section.

Morphological analysis

Reconstruction and preparation for analysis of reconstructed neurons

A total of 20 clusters each containing five to seven PCs and a single IN and five pairs of INs were 3D-reconstructed, tracing them with the FIJI ("FIJI is just ImageJ"; https://imagej.net/Fiji) software package. Image stacks were registered using the Stitching plug-in (*50*), and the reconstructions were made using the Simple Neurite Tracer plug-in (*51*). For the INs, both dendrites and axons were reconstructed, while for the PCs, only the somato-dendritic domains were reconstructed. We excluded NFS INs based on electrophysiological parameters and a linear discriminant analysis as previously described (*38*). In preparation for subsequent analyses, reconstructions were processed in the NEURON environment (*52*). Individual cells and clusters were rotated with the superficial layers facing the 12 o'clock orientation, with the mEC toward the 9 o'clock and the subiculum at 3 o'clock positions. Where necessary, the reconstructions were convolved with a 3D Gaussian kernel (xy: $\sigma = 3$; z: $\sigma = 5$) to smoothen spatial artifacts generated by the semiautomatic tracing process. For cell clusters, we additionally measured the intersomatic distances between reconstructed INs and PCs using the measurement tool in

FIJI. As the individual cells were differentially filled, we considered the intersomatic distance center to center of the respective cell bodies.

Analysis of reconstructed neurons

To assess the distribution of the IN axons in the anatomical space, we generated a density map based on their axonal arbor. For this, we calculated the 3D axon length density (axon length in micrometers per cubic micrometer) with a spatial resolution of 1-μm^3 voxels. The center of the cell body was used as the origin of the coordinate system. The axodendritic overlap score for neighboring biocytin-filled PCs was calculated as the sum of the axonal density values in all 1-μm^3 voxels spatially overlapping with the PC cell body and dendrites. We plotted the representation of the IN with the density cloud, using mayavi 4.5, a 3D visualization package for Python. Specifically, we plotted the density cloud as a volume scalar field and the dendrites and cell body using the inbuilt "points3d" and "triangular_mesh" functions, respectively.

The 3D polar plots were generated using Python 3.7, the astropy 4.1 Python package, and mayavi 4.5. For this, axonal densities were translated from the Cartesian coordinate system into spherical coordinates using the inbuilt astropy "cartesian_to_spherical" function. The axonal representation was normalized by setting the length of the longest vector to the surface to 1, and the data were binned at 10° segments in the elevation and azimuthal planes. The resulting plots were visualized using the "mesh" function on mayavi 4.5. We calculated the polarity index from the binned data by calculating the sum of the variance as the deviation of the calculated direction vectors to the surface from those of a perfect sphere of equal volume and homogeneous density. To further quantify the spatial polarization of the axons, we approximated their distribution as an ellipsoid and quantified their eccentricity. This parameter equates to 0 for a perfect sphere and is between 0 and 1 for an oval ellipsoid and can be calculated as the ratio of the distance between foci and the long axis of the spheroid (*53*)

$$\text{Eccentricity} = \sqrt{1 - \left(\frac{\text{Length of the minor axis}}{\text{Length of the major axis}}\right)^2}$$

All statistical tests were done using GraphPad Prism 8. To examine the distributions of our data samples, we tested for normality (Shapiro-Wilk's normality test) and homoscedasticity (Levene's *F* test). To determine the significance of our samples, we used parametric (Student's *t* test) or nonparametric (Mann-Whitney *U* test) statistic tests respectively, as indicated in the text.

Spatial network model

Code for the generation, simulation, and analysis of the spatial network is available at https://doi.org/10.12751/g-node.abju0s.

Neural sheet

The 2D spatial network is constructed by placing 3600 PCs in a 60 × 60 grid and 400 INs in a 20 × 20 grid on a 900 μm by 900 μm neural sheet. On the basis of this spatial layout, we infer the synaptic connections using the experimentally observed connectivity rule: Each PC covered by an IN's axon is reciprocally connected to the latter (Figs. 2 and 4B). We then compare two connectivity structures: directional inhibition by the here-reported polarized axons and a blanket of inhibition by circular axons. Polarized axons are modeled as ellipsoids with a long half-axis of 100 μm and a short half-axis of 25 μm approximating the dimensions found in the axonal reconstructions (see Fig. 3), whereas circular IN axons are represented by area-equivalent circles with a radius of 50 μm (Fig. 4B). Conservation of the axonal area ensures that the number of synapses and therefore the overall amount of inhibition and excitation remain the same in both networks, simulating a connectivity principle with comparable wiring cost.

Neuron models

PCs are simulated by a conductance-based Hodgkin-Huxley model with sodium, potassium, and leak channels. In addition, they receive a HD-dependent input current $I_{HD}(\theta)$ and inhibitory synaptic currents I_{inh}

$$C_m\dot{v} = -g_L(v - E_L) - g_{Na}m^3h(v - E_{Na}) - g_K n^4(v - E_K) + I_{HD}(\theta) + I_{inh}$$

$$\dot{m} = \frac{0.32}{\text{ms}}\frac{13\,\text{mV} - v + V_T}{\left(e^{\frac{13\,\text{mV}-v+V_T}{4\,\text{mV}}} - 1\right)\text{mV}}(1 - m) - \frac{0.28}{\text{ms}}\frac{v - V_T - 40\,\text{mV}}{\left(e^{\frac{v-V_T-40\,\text{mV}}{5\,\text{mV}}} - 1\right)\text{mV}}m$$

$$\dot{n} = \frac{0.032}{\text{ms}}\frac{15\,\text{mV} - v + V_T}{\left(e^{\frac{15\,\text{mV}-v+V_T}{5\,\text{mV}}} - 1\right)\text{mV}}(1 - n) - \frac{0.5}{\text{ms}}e^{\frac{10\,\text{mV}-v+V_T}{40\,\text{mV}}}n$$

$$\dot{h} = \frac{0.128}{\text{ms}}e^{\frac{17\,\text{mV}-v+V_T}{18\,\text{mV}}}(1 - h) - \frac{4}{\text{ms}}\frac{1}{1 + e^{\frac{40\,\text{mV}-v+V_T}{5\,\text{mV}}}}h$$

A	20,000 μm^2	Neuron area
C_m	$1\frac{\mu F}{cm^2}A$ = 200 pF	Membrane capacitance
g_L	$50\frac{\mu S}{cm^2}A$ = 10 nS	Leak conductance
E_L	−65 mV	Leak reversal potential
E_K	−90 mV	Potassium reversal potential
E_{Na}	50 mV	Sodium reversal potential
g_{Na}	$100\frac{mS}{cm^2}A$ = 20 μS	Sodium conductance
g_K	$30\frac{mS}{cm^2}A$ = 6 μS	Potassium conductance
V_T	−63 mV	Activation shift

INs are modeled as leaky integrate and fire neurons with equilibrium voltage v_{eq}, threshold voltage v_{thres}, reset voltage v_{reset}, and no refractory period

$$\dot{v} = \frac{1}{\tau}(-v + v_{eq})$$

τ	7 ms	Time constant
v_{eq}	−50 mV	Equilibrium voltage
v_{thres}	−40 mV	Threshold voltage
v_{reset}	−60 mV	Reset voltage

Synapse models

An inhibitory synapse is modeled as a conductance $g_{\mathrm{Syn},\,n\mathrm{IE}}$. When the corresponding IN spikes, the conductance is increased by 30 nS and afterward decays with time constant τ_{Syn}. The overall synaptic input current for a PC is then calculated from the sum over all connected INs

$$\dot{g}_{\mathrm{Syn},n_{\mathrm{IE}}} = -\frac{g_{\mathrm{Syn},n_{\mathrm{IE}}}}{\tau_{\mathrm{Syn}}}$$

$$I_{\mathrm{Syn}} = -\left(\sum_{N_{\mathrm{IE}}} g_{\mathrm{Syn},n_{\mathrm{IE}}}\right)(v - E_i)$$

τ_{Syn}	1 ms	Synaptic time constant
Δg_{Syn}	30 nS	Synaptic strength

The IN's synapses are modeled as voltage synapses. At a presynaptic spike, the membrane voltage of the IN is increased by the excitatory synaptic strength $\Delta v_{\mathrm{Syn}} = 2.5$ mV.

HD input: Topology and the max entropy rule

A potential topography of HD tuning is modeled by a HD-modulated input current to every PC. The preferred direction θ_{pref} of a PC depends on its location on the neural sheet (see Fig. 4B and the Spatial organization of HD input: Perlin and pinwheel map section). We consider a static situation, where the HD, i.e., a von Mises distribution

$$I_{\mathrm{HD}}(\theta) = I_{\mathrm{baseline}} + I_{\mathrm{HD}}\frac{e^{\kappa^*\cos(\theta-\theta_{\mathrm{pref}})}}{e^{\kappa}}$$

We choose a broad input profile with dispersion $\kappa = 2.5$ (corresponding to $\sigma^2 = 0.4$), a peak amplitude $I_{\mathrm{HD}} = 0.6$ nA, and an additional uniform baseline of 0.05 nA.

Choosing the directionality of polarized IN axons: Max entropy rule

The spatial orientation of a polarized IN provides an additional degree of freedom. We propose that this axonal orientation is optimized to enhance competition between PCs with different HD preferences and thereby increase the PC's HD tuning. In principle, this poses a complex global and functional optimization problem: Given an input map and the locations of all neurons, find the set of axonal orientations that maximizes the HD tuning of the PC population. Here, we resort to a simpler local and structural optimization. We assume that an IN's axon orientation maximizes the diversity of HD preferences within the group of PCs connected to it. In this way, the IN mediates reciprocal inhibition between a large set of HD preferences. To find the corresponding axon orientation, we maximize the entropy of HD preferences among the connected PCs (fig. S4A). To calculate this entropy for a specific axonal orientation ϕ, we first determine the set of preferred HDs within the connected PCs. From this set of HD preferences, we then determine the binned, normalized histogram of present HD preferences p_θ. We use 30 bins, corresponding to a bin width of 20°. Next, we calculate the entropy of this distribution

$$S_\phi = \sum -p_\theta \log p_\theta$$

The entropy S_ϕ gives a measure for uniformity of probabilities and therefore diversity of preferred tuning directions. For each IN, this entropy measure is calculated for 30 equally spaced orientations ϕ, and the direction of maximum entropy is chosen.

Spatial organization of HD input: Perlin and pinwheel map

As the spatial structure of the thalamic HD input to the PrS is not known, we resort to artificially generated HD preference topologies. These input topologies are represented as spatial maps of HD preference: The location of a PC in the neural sheet determines its preferred HD. We tested two such spatial maps: a Perlin and a pinwheel map.

Perlin/simplex noise is a spatial map originally developed for computer-generated imagery of natural textures (*54*). The organic nature of these textures with local correlations has also found applications in neuroscience (*47*). By introducing a scaling parameter, a Perlin map allows us to vary from a salt-and-pepper topography to a spatially structured input topography (fig. S4C). In the used simplex noise implementation (OpenSimplex for Python), neighboring points on the simplex grid are a distance of $\sqrt{2}$ μm apart, setting an upper bound for spatial correlation on the map. The size of spatial structures is varied by scaling the input coordinates of the noise function noise2D(x/scale, y/scale). Since simplex noise is centered on zero, certain HD preferences are strongly overrepresented. A uniform distribution of HDs is achieved by reassigning the sorted, previously generated noise values to equidistant values between $-\pi$ and π (*47*).

To show that the results are robust with respect to the choice of spatial map, we also tested a pinwheel map (fig. S4D), originally developed as a model for the topology of orientation preference in the visual cortex (*55*). This pinwheel map is generated by assigning each PC on the 60 × 60 grid a randomly oriented vector of length $\sqrt{2}/100$. The orientation of the vector represents the preferred tuning direction of the PC. Spatial correlations are created by iteratively comparing and adjusting the vectors to their neighbors in a certain region, similar to the alignment of nearby magnets. For each vector $\mathbf{z}_i$, every other vector $\mathbf{z}_j$ is added if its distance on the grid is closer than $c/2$, subtracted if its distance is within $c/2$ and c, and disregarded otherwise, with c as the scaling parameter. Larger c value leads to larger patches of similar HD tuning, while low values of c essentially lead to a salt-and-pepper topography. If the length of a vector reaches 1, it remains unchanged. This is repeated for five iterations. The map is subsequently adjusted in the same way as the simplex map to guarantee a uniform distribution of tuning values.

Correlation length

To quantify the size of spatial structures on these input maps, a correlation length of HD preference is calculated (fig. S4, C and D). For every possible grid-wise displacement of the map to itself, a circular correlation is calculated from the overlapping region (Python package pingouin). Note that the distribution of input directions is uniform at least for the entire map and close to uniform for large subsections, requiring an adaptation of the circular mean for uniform distributions (*56*). The acquired correlation values are binned by their respective displacement distances and averaged per bin with a binning width of 3 μm. The resulting mean autocorrelation per distance is fitted by a single exponential function, leading to the correlation length. Averaging the correlation length for the 10 different input maps generated per grid scale leads to the correlation length scale in Fig. 4F.

Analysis of HD tuning

The full network of 3600 PCs and 400 INs is simulated for 1 s using the spiking network simulator Brian 2 (*57*) in conjunction with the

parameter exploration package pypet (*58*). Three different network setups are compared: polarized INs, circular INs, and a control network without synaptic connections (Fig. 4B). We test 24 spatial input map scales resulting in input maps from a correlation length of zero with salt-and-pepper topography up to a correlation length of 125 μm where the spatial topography is larger than the long axis of the polarized INs. Note that, for each input map, the axonal directions of the polarized INs have to be adjusted according to the maximum entropy rule. For each input map scale, the three networks are simulated for 12 different HDs and 10 input map instances each (fig. S4). From the interspike intervals, a firing rate is calculated for each neuron. The tuning of the network is analyzed by calculating the HDI (see the "HD index" section) for each individual neuron (Fig. 4C), excluding those with a distance of less than 100 μm from the edge of the sheet to counteract border effects. Next, the distribution of HDIs of the excitatory and inhibitory populations with their respective means is computed for each map (Fig. 4E). Last, for each input scale, 10 different input maps are used to determine the average and SD of these mean HDIs and compare their behavior when varying the input topography (Fig. 4F). The correlation length corresponding to this input scale is also averaged across the 10 maps, as described above.

HD index

The HDI is used as a measure of the sharpness of individual cell tuning (*59*). It is calculated by constructing a vector in each of the 12 input directions ϕ_i with its length equal to the associated firing rate of the cell $\mathrm{fr}(\phi_i)$ in that direction

$$\mathbf{z}_i = \mathrm{fr}(\phi_i)\begin{pmatrix}\cos(\phi_i)\\ \sin(\phi_i)\end{pmatrix}$$

The vectors are normalized by the sum of all firing rates and added together, forming a tuning vector that points in the direction of preferred tuning

$$\mathbf{z} = \frac{\sum_i \mathbf{z}_i}{\sum_i \mathrm{fr}(\phi_i)}$$

The tuning vector length $|\mathbf{z}|$ indicates the sharpness of this particular neuron tuning, increasing from zero (no tuning to HD) to one (only firing in one direction).

SUPPLEMENTARY MATERIALS

Supplementary material for this article is available at http://advances.sciencemag.org/cgi/content/full/7/25/eabg4693/DC1

View/request a protocol for this paper from *Bio-protocol*.

REFERENCES AND NOTES

1. R. Perin, T. K. Berger, H. Markram, A synaptic organizing principle for cortical neuronal groups. *Proc. Natl. Acad. Sci. U.S.A.* **108**, 5419–5424 (2011).
2. S. Song, P. Sjöström, M. Reigl, S. Nelson, D. B. Chklovskii, Highly nonrandom features of synaptic connectivity in local cortical circuits. *PLOS Biol.* **3**, e68 (2005).
3. A. M. Packer, R. Yuste, Dense, unspecific connectivity of neocortical parvalbumin-positive interneurons: A canonical microcircuit for inhibition? *J. Neurosci.* **31**, 13260–13271 (2011).
4. A. Peters, M. L. Feldman, The projection of the lateral geniculate nucleus to area 17 of the rat cerebral cortex. I. General description. *J. Neurocytol.* **5**, 63–84 (1976).
5. G. M. G. Shepherd, A. Stepanyants, I. Bureau, D. Chklovskii, K. Svoboda, Geometric and functional organization of cortical circuits. *Nat. Neurosci.* **8**, 782–790 (2005).
6. A. M. Packer, D. J. McConnell, E. Fino, R. Yuste, Axo-dendritic overlap and laminar projection can explain interneuron connectivity to pyramidal cells. *Cereb. Cortex* **23**, 2790–2802 (2013).
7. E. Fino, A. M. Packer, R. Yuste, The logic of inhibitory connectivity in the neocortex. *Neuroscientist* **19**, 228–237 (2013).
8. J. S. Isaacson, M. Scanziani, How inhibition shapes cortical activity. *Neuron* **72**, 231–243 (2011).
9. H. Hu, J. Gan, P. Jonas, Fast-spiking, parvalbumin$^+$ GABAergic interneurons: From cellular design to microcircuit function. *Science* **345**, 1255263 (2014).
10. C. Espinoza, S. Guzman, X. Zhang, P. Jonas, Parvalbumin$^+$ interneurons obey unique connectivity rules and establish a powerful lateral-inhibition microcircuit in dentate gyrus. *Nat. Commun.* **9**, 4605 (2018).
11. S. Rieubland, A. Roth, M. Häusser, Structured connectivity in cerebellar inhibitory networks. *Neuron* **81**, 913–929 (2014).
12. C. Schmidt-Hieber, M. Häusser, Cellular mechanisms of spatial navigation in the medial entorhinal cortex. *Nat. Neurosci.* **16**, 325–331 (2013).
13. R. Milo, S. Shen-Orr, S. Itzkovitz, N. Kashtan, D. Chklovskii, U. Alon, Network motifs: Simple building blocks of complex networks. *Science* **298**, 824–827 (2002).
14. D. E. Wilson, B. Scholl, D. Fitzpatrick, Differential tuning of excitation and inhibition shapes direction selectivity in ferret visual cortex. *Nature* **560**, 97–101 (2018).
15. D. E. Wilson, G. B. Smith, A. L. Jacob, T. Walker, J. Dimidschstein, G. Fishell, D. Fitzpatrick, GABAergic neurons in ferret visual cortex participate in functionally specific networks. *Neuron* **93**, 1058–1065.e4 (2017).
16. B. V. Atallah, W. Bruns, M. Carandini, M. Scanziani, Parvalbumin-expressing interneurons linearly transform cortical responses to visual stimuli. *Neuron* **73**, 159–170 (2012).
17. S.-H. Lee, A. C. Kwan, S. Zhang, V. Phoumthipphavong, J. G. Flannery, S. C. Masmanidis, H. Taniguchi, Z. J. Huang, F. Zhang, E. S. Boyden, K. Deisseroth, Y. Dan, Activation of specific interneurons improves V1 feature selectivity and visual perception. *Nature* **488**, 379–383 (2012).
18. P. Znamenskiy, M.-H. Kim, D. R. Muir, M. F. Iacaruso, S. B. Hofer, T. D. Mrsic-Flogel, Functional selectivity and specific connectivity of inhibitory neurons in primary visual cortex. *Biorxiv* , 294835 (2018).
19. S. B. Hofer, H. Ko, B. Pichler, J. Vogelstein, H. Ros, H. Zeng, E. Lein, N. A. Lesica, T. D. Mrsic-Flogel, Differential connectivity and response dynamics of excitatory and inhibitory neurons in visual cortex. *Nat. Neurosci.* **14**, 1045–1052 (2011).
20. L. F. Rossi, K. D. Harris, M. Carandini, Spatial connectivity matches direction selectivity in visual cortex. *Nature* , 648–652 (2020).
21. A. Peyrache, A. J. Duszkiewicz, G. Viejo, S. Angeles-Duran, Thalamocortical processing of the head-direction sense. *Prog. Neurobiol.* **183**, 101693 (2019).
22. A. Peyrache, N. Schieferstein, G. Buzsáki, Transformation of the head-direction signal into a spatial code. *Nat. Commun.* **8**, 1752 (2017).
23. G. Viejo, A. Peyrache, Precise coupling of the thalamic head-direction system to hippocampal ripples. *Nat. Commun.* **11**, 2524 (2020).
24. J. S. Taube, The head direction signal: Origins and sensory-motor integration. *Annu. Rev. Neurosci.* **30**, 181–207 (2007).
25. J. J. Tukker, Q. Tang, A. Burgalossi, M. Brecht, Head-directional tuning and theta modulation of anatomically identified neurons in the presubiculum. *J. Neurosci.* **35**, 15391–15395 (2015).
26. P. Preston-Ferrer, S. Coletta, M. Frey, A. Burgalossi, Anatomical organization of presubicular head-direction circuits. *eLife* **5**, e14592 (2016).
27. M. Nassar, J. Simonnet, L.-W. Huang, B. Mathon, I. Cohen, M. H. Bendels, M. Beraneck, R. Miles, D. Fricker, Anterior thalamic excitation and feedforward inhibition of presubicular neurons projecting to medial entorhinal cortex. *J. Neurosci.* **38**, 6411–6425 (2018).
28. I. Zutshi, M. L. Fu, V. Lilascharoen, J. K. Leutgeb, B. Lim, S. Leutgeb, Recurrent circuits within medial entorhinal cortex superficial layers support grid cell firing. *Nat. Commun.* **9**, 3701 (2018).
29. J. J. Couey, A. Witoelar, S.-J. Zhang, K. Zheng, J. Ye, B. Dunn, R. Czajkowski, M.-B. Moser, E. I. Moser, Y. Roudi, M. P. Witter, Recurrent inhibitory circuitry as a mechanism for grid formation. *Nat. Neurosci.* **16**, 318–324 (2013).
30. H. Pastoll, L. Solanka, M. van Rossum, M. F. Nolan, Feedback inhibition enables theta-nested gamma oscillations and grid firing fields. *Neuron* **77**, 141–154 (2013).
31. O. Shipston-Sharman, L. Solanka, M. F. Nolan, Continuous attractor network models of grid cell firing based on excitatory–inhibitory interactions. *J. Physiol.* **594**, 6547–6557 (2016).
32. J. Simonnet, M. Nassar, F. Stella, I. Cohen, B. Mathon, C. N. Boccara, R. Miles, D. Fricker, Activity dependent feedback inhibition may maintain head direction signals in mouse presubiculum. *Nat. Commun.* **8**, 16032 (2017).
33. P. Song, X.-J. Wang, Angular path integration by moving "Hill of Activity": A spiking neuron model without recurrent excitation of the head-direction system. *J. Neurosci.* **25**, 1002–1014 (2005).
34. S. S. Kim, H. Rouault, S. Druckmann, V. Jayaraman, Ring attractor dynamics in the *Drosophila* central brain. *Science* **356**, 849–853 (2017).
35. Y. E. Fisher, J. Lu, I. D'Alessandro, R. I. Wilson, Sensorimotor experience remaps visual input to a heading-direction network. *Nature* **576**, 121–125 (2019).

36. S. S. Kim, A. M. Hermundstad, S. Romani, L. F. Abbott, V. Jayaraman, Generation of stable heading representations in diverse visual scenes. *Nature* **576**, 126–131 (2019).
37. M. Brecht, S. Ray, A. Burgalossi, Q. Tang, H. Schmidt, R. Naumann, An isomorphic mapping hypothesis of the grid representation. *Philos. Trans. R. Soc. Lond. B Biol. Sci.* **369**, 20120521 (2014).
38. Y. Peng, F. J. Tomás, C. Klisch, I. Vida, J. R. Geiger, Layer-specific organization of local excitatory and inhibitory synaptic connectivity in the rat presubiculum. *Cereb. Cortex* **27**, 2435–2452 (2017).
39. L. Zhao, B. Beverlin II, T. Netoff, D. Q. Nykamp, Synchronization from second order network connectivity statistics. *Front. Comput. Neurosci.* **5**, 28 (2011).
40. S. Grosser, F. J. Barreda, P. Beed, D. Schmitz, S. A. Booker, I. Vida, Parvalbumin interneurons are differentially connected to principal cells in inhibitory feedback microcircuits along the dorsoventral axis of the medial entorhinal cortex. *eNeuro.* **8**, ENEURO.0354-20.2020 (2021).
41. E. Fino, R. Yuste, Dense inhibitory connectivity in neocortex. *Neuron* **69**, 1188–1203 (2011).
42. A. Gour, K. M. Boergens, N. Heike, Y. Hua, P. Laserstein, K. Song, M. Helmstaedter, Postnatal connectomic development of inhibition in mouse barrel cortex. *Science* **371**, eabb4534 (2020).
43. O. Mackwood, L. B. Naumann, H. Sprekeler, Learning excitatory-inhibitory neuronal assemblies in recurrent networks. *Biorxiv* 2020.03.30.016352 , (2020).
44. S. Peron, R. Pancholi, B. Voelcker, J. D. Wittenbach, H. F. Ólafsdóttir, J. Freeman, K. Svoboda, Recurrent interactions in local cortical circuits. *Nature* **579**, 256–259 (2020).
45. S. N. Chettih, C. D. Harvey, Single-neuron perturbations reveal feature-specific competition in V1. *Nature* **567**, 334–340 (2019).
46. L. Acharya, Z. M. Aghajan, C. Vuong, J. J. Moore, M. R. Mehta, Causal influence of visual cues on hippocampal directional selectivity. *Cell* **164**, 197–207 (2016).
47. S. Spreizer, A. Aertsen, A. Kumar, From space to time: Spatial inhomogeneities lead to the emergence of spatiotemporal sequences in spiking neuronal networks. *PLOS Comput. Biol.* **15**, e1007432 (2019).
48. M. Uematsu, Y. Hirai, F. Karube, S. Ebihara, M. Kato, K. Abe, K. Obata, S. Yoshida, M. Hirabayashi, Y. Yanagawa, Y. Kawaguchi, Quantitative chemical composition of cortical GABAergic neurons revealed in transgenic venus-expressing rats. *Cereb. Cortex* **18**, 315–330 (2008).
49. Y. Benjamini, Y. Hochberg, Controlling the false discovery rate: A practical and powerful approach to multiple testing. *J. R. Statis. Soc. B* **57**, 289–300 (1995).
50. S. Preibisch, S. Saalfeld, P. Tomancak, Globally optimal stitching of tiled 3D microscopic image acquisitions. *Bioinformatics* **25**, 1463–1465 (2009).
51. M. H. Longair, D. A. Baker, D. J. Armstrong, Simple Neurite Tracer: Open source software for reconstruction, visualization and analysis of neuronal processes. *Bioinformatics* **27**, 2453–2454 (2011).
52. M. L. Hines, N. T. Carnevale, The NEURON simulation environment. *Neural Comput.* **9**, 1179–1209 (1997).
53. G. Thomas, R. Finnley, *Calculus and Analytic Geometry* (Addison-Wesley Publishers Limited, ed. 7, 1988), 1136 pp.
54. K. Perlin, An image synthesizer. *ACM Siggraph Comput Graph.* **19**, 287–296 (1985).
55. N. V. Swindale, A model for the formation of orientation columns. *Proc. R. Soc. B Biol. Sci.* **215**, 211–230 (1982).
56. S. R. Jammalamadaka, A. SenGupta, *Topics in Circular Statistics* (2001), vol. 5, 336 pp.
57. M. Stimberg, R. Brette, D. F. M. Goodman, Brian 2, an intuitive and efficient neural simulator. *eLife* **8**, e47314 (2019).
58. R. Meyer, K. Obermayer, *pypet*: A python toolkit for data management of parameter explorations. *Front. Neuroinform.* **10**, 38 (2016).
59. A. Burgalossi, L. Herfst, M. von Heimendahl, H. Förste, K. Haskic, M. Schmidt, M. Brecht, Microcircuits of functionally identified neurons in the rat medial entorhinal cortex. *Neuron* **70**, 773–786 (2011).

Acknowledgments: We thank J. Simonnet and J. Bischofberger for comments on the manuscript; H. Sprekeler, L. Naumann, and O. Mackwood for discussions on the network model; and S. Spreizer for the code of Perlin noise generation. VGAT-Venus transgenic rats were generated by Y. Yanagawa, M. Hirabayashi, and Y. Kawaguchi in the National Institute for Physiological Sciences, Okazaki, Japan, using pCS2-Venus provided by A. Miyawaki. **Funding:** This research was supported by the Deutsche Forschungsgemeinschaft (FOR 2143: GE 1175/2-2, VI 353-1/2; GRK 1589), Federal Ministry of Education and Research Germany (01GQ 1403), and the European Research Council (Consolidator grant no. 864243). **Author contributions:** J.R.P.G. and Y.P. developed initial ideas. Y.P., F.J.B.T., I.V., and J.R.P.G. designed the experiments. Y.P. performed the multi–patch-clamp recordings and analysis. F.J.B.T. performed the single-cell patch-clamp recordings, 3D reconstructions, and morphological analysis. M.D., P.P., and S.S. developed the spatial network model. M.D. and P.P. simulated and analyzed the network model. All authors contributed to the interpretation of the results and writing of the final manuscript. **Competing interests:** The authors declare that they have no competing interests. **Data and materials availability:** All data needed to evaluate the conclusions in the paper are present in the paper and/or the Supplementary Materials. The dataset and code used to analyze the network motifs, interneuron degree distribution, axonal overlap scores, and axon polarity are available on Zenodo: https://doi.org/10.5281/zenodo.4670433. The 3D anatomical reconstructions of the neurons are available on the http://neuromorpho.org platform. The code used to generate the spatial network models is available at https://doi.org/10.12751/g-node.abju0s. Additional data related to this paper may be requested from the authors.

Submitted 7 January 2021
Accepted 4 May 2021
Published 16 June 2021
10.1126/sciadv.abg4693

Citation: Y. Peng, F. J. Barreda Tomas, P. Pfeiffer, M. Drangmeister, S. Schreiber, I. Vida, J. R. P. Geiger, Spatially structured inhibition defined by polarized parvalbumin interneuron axons promotes head direction tuning. *Sci. Adv.* **7**, eabg4693 (2021).